Results in Physics 6 (2016) 428–433

Contents lists available at ScienceDirect

Results in Physics

journal homepage: www.journals.elsevier.com/results-in-physics

Texture inheritance from austenite to 7 M martensite in Ni–Mn–Ga melt-spun ribbons

Zongbin Li [a,*], Yiwen Jiang [a], Zhenzhuang Li [a], Yiqiao Yang [a], Bo Yang [a], Yudong Zhang [b,c], Claude Esling [b,c], Xiang Zhao [a], Liang Zuo [a,d,*]

[a] Key Laboratory for Anisotropy and Texture of Materials (Ministry of Education), School of Material Science and Engineering, Northeastern University, Shenyang 110819, China
[b] Laboratoire d'Étude des Microstructures et de Mécanique des Matériaux (LEM3), CNRS UMR 7239, Université de Lorraine, 57045 Metz, France
[c] Laboratory of Excellence on Design of Alloy Metals for low-mAss Structures (DAMAS), Université de Lorraine, 57045 Metz, France
[d] Taiyuan University of Science and Technology, Taiyuan 030024, China

ARTICLE INFO

Article history:
Received 13 June 2016
Accepted 28 July 2016
Available online 2 August 2016

Keywords:
Ni–Mn–Ga ribbons
Martensitic transformation
Texture
Crystallography

ABSTRACT

In this work, $Ni_{53}Mn_{22}Ga_{25}$ and $Ni_{51}Mn_{27}Ga_{22}$ ribbons with austenite and 7 M martensite at room temperature respectively, were prepared by melt-spinning. Through the detailed crystallographic analyses, the preferred orientation in ribbons was confirmed. It is shown that the austenite in $Ni_{53}Mn_{22}Ga_{25}$ ribbons forms a preferred orientation with $\{400\}_A$ in parallel to ribbon plane, whereas the 7 M martensite in $Ni_{51}Mn_{27}Ga_{22}$ ribbons develops the preferred orientation with $\{20\bar{2}0\}_{7M}$, $\{2020\}_{7M}$, and $\{040\}_{7M}$ crystallographic planes parallel to the ribbon plane. Since $\{20\bar{2}0\}_{7M}$, $\{2020\}_{7M}$, and $\{040\}_{7M}$ are originated from $\{400\}_A$, the preferred orientation in ribbons thus can be inherited after the martensitic transformation. Such texture inheritance is attributed to the intrinsic orientation relationship between austenite and 7 M martensite.

Introduction

Due to the strong coupling between the magnetic and structural orders in Ni–Mn–Ga ferromagnetic shape memory alloys [1–3], large magnetic field induced strain (i.e. magnetic shape memory effect) can be obtained through the field induced variant reorientation [4]. It is noted that the field needed to drive the variant reorientation in Ni–Mn–Ga alloys is smaller ($\leqslant$1T) than that to realize the field induced phase transformation in Ni–Mn–In or Ni–Mn–Sn based alloys [5]. In contrast to the conventional shape memory alloys with slow dynamic response that is restricted by the thermal activation, Ni–Mn–Ga alloys combine large output and fast dynamic response under the actuation of external magnetic field. Thus, these alloys are viewed as a new class of the smart material and can be developed as the potential candidates for the applications in actuators and sensors.

In general, Ni–Mn–Ga alloys undergo a first-order diffusionless martensitic transformation from high-symmetric cubic $L2_1$ ordered austenite to low-symmetric martensite on cooling. Depending on the chemical composition, two types of martensite, namely modulated (e.g., five-layered (5 M), seven-layered (7 M)) and non-modulated (NM) martensite, are frequently observed [6]. So far, large magnetic field induced strains up to ~7.1%, ~11.2% and ~12% have been reported in single crystals with 5 M martensite, 7 M martensite and NM martensite [7–9], respectively. However, the relatively high fabricating cost of single crystals represents a major obstacle for the practical application. In contrast, the manufacturing of polycrystalline alloys is much simpler and easier to be implemented, but the random distribution of the crystallographic orientation in polycrystallines greatly weakens the field induced functional behaviors. To improve the functional properties in polycrystalline alloys, a highly textured microstructure is of great significance.

Recently, the rapid solidification based on melt-spinning technique has been proven to be an effective single-step processing route for the preparation of ferromagnetic shape memory alloys [10–19], which significantly reduces the consuming of long time post heat treatment to achieve the composition homogeneity. Moreover, melt-spun ribbons usually tend to form a highly textured microstructure. It is shown that the austenite of the Ni–Mn–Ga alloy in melt-spun ribbons tends to exhibit a preferred distribution with $\{400\}_A$ parallel to the ribbon plane [18]. However, the situation in martensite seems to be more complicated.

* Corresponding authors at: Key Laboratory for Anisotropy and Texture of Materials (Ministry of Education), School of Material Science and Engineering, Northeastern University, Shenyang 110819, China (Z.B. Li and L. Zuo).
E-mail addresses: lizongbin@126.com (Z. Li), lzuo@mail.neu.edu.cn (L. Zuo).

http://dx.doi.org/10.1016/j.rinp.2016.07.012
2211-3797/

On the one hand, the crystallographic symmetry of martensite is much lower than austenite and on the other hand, one austenite grain may generate at most 24 martensite variants after the phase transformation. So far, the preferred orientation distribution of martensite in melt-spun ribbons has not been reported, and its crystallographic correlation to austenite orientation still needs to be further explored. Deep insights into the crystallographic correlation of the orientation distribution between austenite and martensite in melt-spun ribbons are of great significance for microstructure control and further property optimization.

In this work, two ribbon samples (i.e. $Ni_{53}Mn_{22}Ga_{25}$ and $Ni_{51}Mn_{27}Ga_{22}$) with austenite and 7 M martensite at room temperature respectively, were prepared by melt-spinning. Through the detailed analyses on the crystallographic texture in ribbons, we found that there existed a strong texture inheritance from austenite to 7 M martensite and such inheritance of the preferred orientation should be attributed to the intrinsic orientation relationship between the two structural phases.

Experimental

Bulk polycrystalline Ni–Mn–Ga alloys with the nominal compositions of $Ni_{53}Mn_{22}Ga_{25}$ and $Ni_{51}Mn_{27}Ga_{22}$ (at.%) were prepared by arc-melting. The as-cast ingots were remelted four times to achieve a good composition homogeneity. Ribbons were produced in a single-roller melt-spinning apparatus with a copper wheel rotating speed of 15 m/s, using the as-cast alloys as the master materials. The ribbon plane of the melt-spun ribbons was electrolytically polished with a solution of 20% nitric acid in methanol at room temperature in order to perform the microstructural observation.

The martensitic transformation temperatures were determined by differential scanning calorimetry (DSC), using a TA Q100 setup. DSC curves were recorded from 183 to 473 K with a heating and cooling rate of 10 K/min. The phase constitution and the crystal structure of the ribbons were identified by X-ray diffraction (XRD) with Cu-K_α radiation in a PANalytical X'Pert Pro MPD diffractometer at room temperature. The microstructural characterization was performed in a field emission gun scanning electron microscope (SEM, Jeol JSM 6500 F) with an electron backscatter diffraction (EBSD) acquisition camera and Channel 5 software. The texture of the austenite in $Ni_{53}Mn_{22}Ga_{25}$ ribbons was characterized by EBSD mapping, where the "beam control" mode was applied for automated orientation measurements with a step size of 0.4 μm. The texture of the 7 M martensite in $Ni_{51}Mn_{27}Ga_{22}$ ribbons was measured by XRD with a rotating anode generator (RIGAKU RU300) and a large-angle position sensitive detector (INEL CPS120), where the measurements were conducted at tilt angle ψ from 1.25° to 78.75° with a step size of 2.5°. At each tilt angle, the sample was rotated from 0° to 360° with a step size of 5°. For both EBSD and XRD measurements, the pole figures were recalculated by MTEX toolbox [20].

Results

DSC measurements were used to determine the martensitic transformation temperatures of the ribbons. Fig. 1a displays the DSC curves for $Ni_{53}Mn_{22}Ga_{25}$ and $Ni_{51}Mn_{27}Ga_{22}$ ribbons. In the figure, the large exothermic (endothermic) peaks correspond to the forward (reverse) martensitic transformation and the separated small steps of different sign observed almost at the same temperature on the heating and cooling pathways of the curves correspond to the paramagnetic-to-ferromagnetic transition of austenite. Through the tangent method, the martensitic transformation temperatures (M_s, M_f, A_s, A_f) of two ribbon samples were

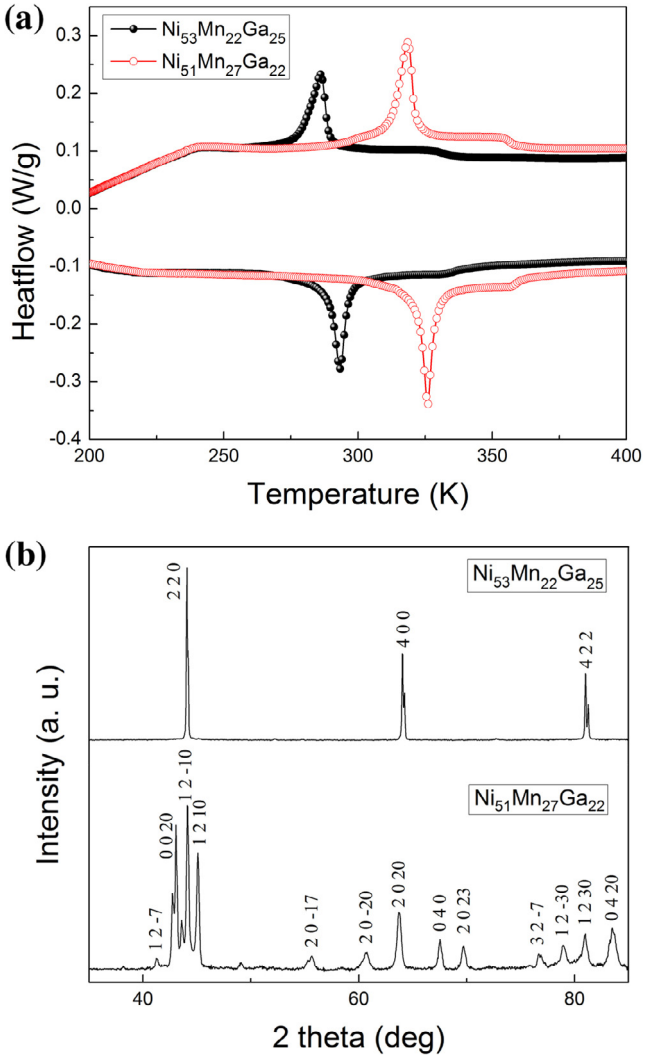

Fig. 1. (a) DSC curves for $Ni_{53}Mn_{22}Ga_{25}$ and $Ni_{51}Mn_{27}Ga_{22}$ ribbons. (b) Room temperature XRD patterns of $Ni_{53}Mn_{22}Ga_{25}$ and $Ni_{51}Mn_{27}Ga_{22}$ ribbons.

well determined from the DSC curves, as shown in Table 1. Apparently, the martensitic transformation temperatures of $Ni_{53}Mn_{22}Ga_{25}$ and $Ni_{51}Mn_{27}Ga_{22}$ ribbons are below and above room temperature, respectively.

Fig. 1b shows the room temperature XRD patterns of $Ni_{53}Mn_{22}Ga_{25}$ and $Ni_{51}Mn_{27}Ga_{22}$ ribbons. According to the XRD patterns, the room temperature phase of $Ni_{53}Mn_{22}Ga_{25}$ ribbons is determined to be austenite with cubic $L2_1$ structure ($a_A = 5.814$ Å), which is consistent with the DSC results. The peak splitting presented in the XRD pattern could be attributed to the $K_{\alpha 2}$ diffraction. For the $Ni_{51}Mn_{27}Ga_{22}$ ribbons, it is found that the ribbons consist of 7 M martensite ($a_{7M} = 4.235$ Å, $b_{7M} = 5.552$, $c_{7M} = 42.061$, $\beta = 92.5°$) at room temperature, where the crystal structure can be depicted as a monoclinic superstructure with incommensurate modulation [21]. By comparison of the respective diffraction peaks for

Table 1
Martensitic transformation temperatures for $Ni_{53}Mn_{22}Ga_{25}$ and $Ni_{51}Mn_{27}Ga_{22}$ ribbons.

Sample	M_s [K]	M_f [K]	A_s [K]	A_f [K]
$Ni_{53}Mn_{22}Ga_{25}$	290	276	286	298
$Ni_{51}Mn_{27}Ga_{22}$	323	308	318	331

austenite and 7 M martensite, it can be inferred that $(220)_A$ diffraction would evolve into $(0020)_{7M}$, $(12\bar{1}0)_{7M}$ and $(1\bar{2}10)_{7M}$, whereas $(400)_A$ into $(20\bar{2}0)_{7M}$, $(2020)_{7M}$ and $(040)_{7M}$, after the transformation from austenite to 7 M martensite.

Fig. 2a shows the EBSD orientation map measured from ribbon plane for the $Ni_{53}Mn_{22}Ga_{25}$ ribbons. It is shown that the austenite grain appears in equiaxed shape with an average grain size of ~10–20 μm. Notably, the melt-spun technique has rendered the austenite grains greatly reduced in size due to an ultra high cooling rate. Fig. 2b displays the corresponding $\{220\}_A$, $\{400\}_A$ and $\{422\}_A$ pole figures recalculated from EBSD measurements. It is obvious that the austenite develops a preferred orientation with $\{400\}_A$ in parallel to ribbon plane, which is consistent with previous study [18]. It is known that the $\langle 001\rangle_A$ crystallographic direction of Ni–Mn–Ga austenite is the preferred crystal growth direction along the thermal gradient direction [22]. During the process of the melt-spinning, the radial direction of the copper wheel is a main heat radiating direction or thermal gradient direction [23]. Therefore, nuclei with $\langle 001\rangle_A$ perpendicular to the ribbon plane have the highest privilege to grow, which results in the formation of preferred orientation with $\{400\}_A$ parallel to ribbon plane.

Fig. 3a displays a typical backscattered electron (BSE) image taken on the ribbon plane for $Ni_{51}Mn_{27}Ga_{22}$ ribbons. It is seen that the martensite appears in plate shape. In comparison with the bulk alloys, the plate thickness in ribbons is also greatly reduced, with an averaged plate thickness of ~200–300 nm. Further EBSD measurements show that there are four types of martensitic variants distributed alternately within one variant colony and they are twin-related to each other with three types of twin relationship (type-I twin, type-II twin and compound twin), which is consistent with our previous result on bulk alloys [21]. Fig. 3b shows the room temperature secondary electron image taken from the cross section perpendicular to the ribbon plane. It is evident that the original austenite grains are in columnar shape, with the long axes

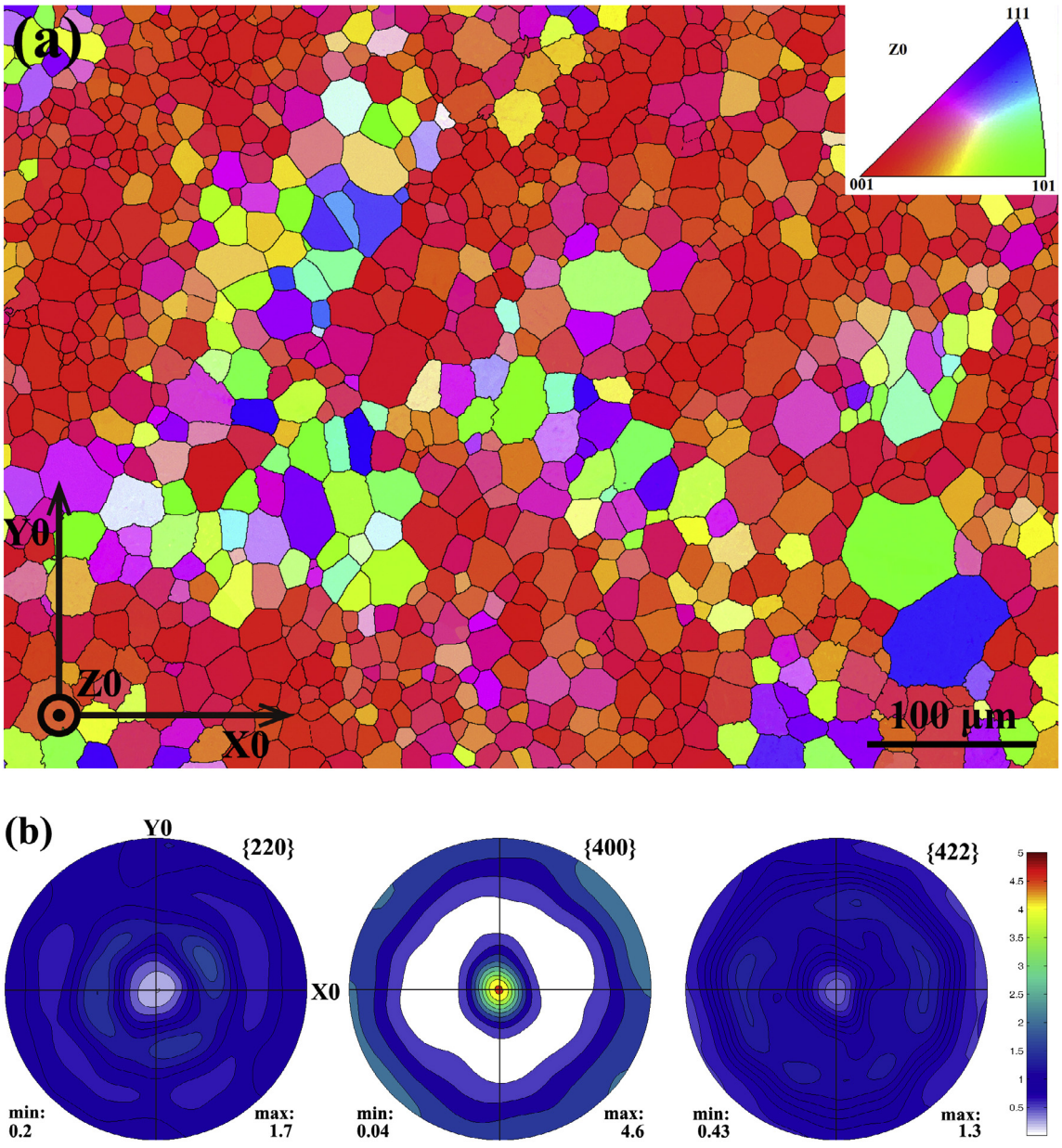

Fig. 2. (a) EBSD orientation map of ribbon plane for the $Ni_{53}Mn_{22}Ga_{25}$ ribbons. (b) Corresponding $\{220\}_A$, $\{400\}_A$ and $\{422\}_A$ pole figures. X0//ribbon length (rolling) direction, Z0⊥ribbon plane.

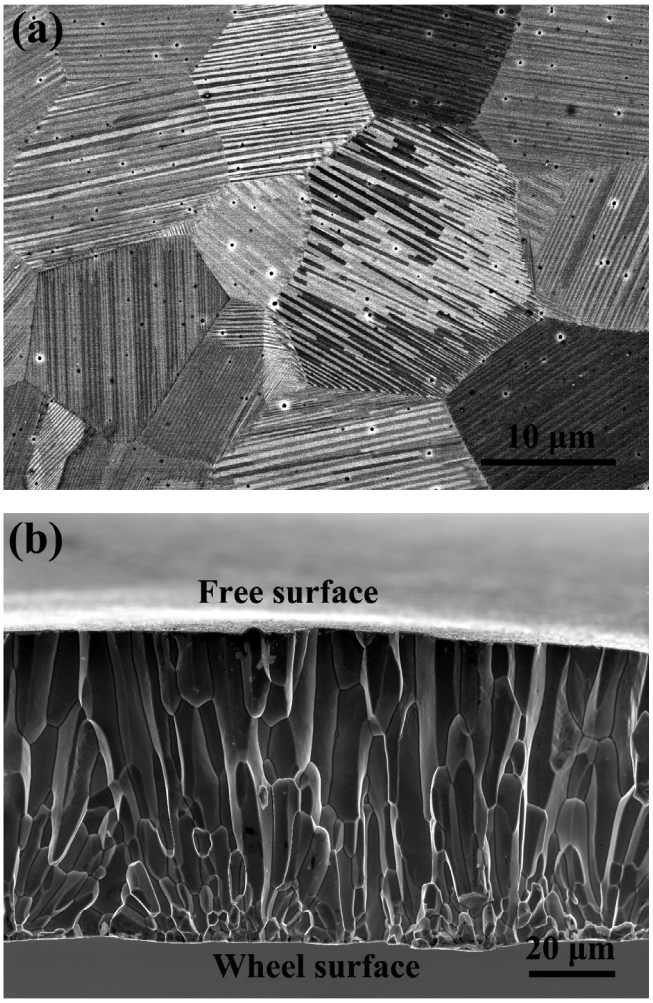

Fig. 3. (a) BSE image of the ribbon plane for $Ni_{51}Mn_{27}Ga_{22}$ ribbons. (b) Microstructure of cross section perpendicular to the ribbon plane.

approximately parallel to the ribbon plane normal. In addition, the grain size of the original austenite at the ribbon surface in contact with the wheel is much smaller than that at the free surface. This morphology should be attributed to the specific heat transfer condition of the melt-spinning process [23].

Since the thickness of martensite plates in melt-spun ribbons is greatly reduced, the indexation rate through the automatic EBSD measurements in a relatively large area is too low to perform a reliable texture analysis on 7 M martensite. Alternatively, to achieve the statistical purpose, XRD was employed to measure the preferred orientation of 7 M martensite. Results show that there exists a strong preferred orientation in $Ni_{51}Mn_{27}Ga_{22}$ ribbons with $\{20\bar{2}0\}_{7M}$, $\{2020\}_{7M}$, and $\{040\}_{7M}$ of 7 M martensite in parallel to the ribbon plane. Fig. 4 shows the corresponding $\{20\bar{2}0\}_{7M}$, $\{2020\}_{7M}$, and $\{040\}_{7M}$ pole figures recalculated from the XRD measurements. It can be seen that the highest intensity in $\{20\bar{2}0\}_{7M}$, $\{2020\}_{7M}$, and $\{040\}_{7M}$ pole figures is located at around the center position, suggesting that $\{20\bar{2}0\}_{7M}$, $\{2020\}_{7M}$, and $\{040\}_{7M}$ tend to be parallel to the ribbon plane. Since $\{20\bar{2}0\}_{7M}$, $\{2020\}_{7M}$, and $\{040\}_{7M}$ planes of 7 M martensite are originated from $\{400\}_A$ of austenite, it can be inferred that the preferred orientation in the ribbons can be inherited after the martensitic transformation. In addition, it is noted in Fig. 4 that the $\{2020\}_{7M}$ pole figure shows the highest maximum intensity. This could be due to the less lattice distortion of $\{2020\}_{7M}$ with respect to $\{400\}_A$. To illustrate this point, we suppose the lattice constant of austenite in $Ni_{51}Mn_{27}Ga_{22}$ ribbons to be $a_A = 5.814$ Å (same to $Ni_{53}Mn_{22}Ga_{25}$ ribbons). The planar spacing of $\{400\}_A$ is determined to be 1.454 Å. On the other hand, the planar spacing of $\{20\bar{2}0\}_{7M}$, $\{2020\}_{7M}$, and $\{0\ 4\ 0\}_{7M}$ for 7 M martensite is 1.524 Å, 1.459 Å and 1.388 Å, respectively. Apparently, the planar spacing of $\{2020\}_{7M}$ is much closer to that of $\{400\}_A$. Therefore, the formation of $\{2020\}_{7M}$ evolved from $\{400\}_A$ is more favored through the collective atomic movements since less lattice distortion is involved, resulting in the relatively high degree of preferred orientation for $\{2020\}_{7M}$.

Discussions

It is noted that both the two ribbon samples (i.e. $Ni_{53}Mn_{22}Ga_{25}$ or $Ni_{51}Mn_{27}Ga_{22}$) are prepared by melt-spinning with the same processing parameters and they exhibit similar morphological feature (i.e., in columnar shape with the long axes approximately parallel to the ribbon plane normal) for the austenite. The difference between two ribbon samples lies in the martensitic transformation temperatures. However, the characteristic transformation temperatures for the $Ni_{51}Mn_{27}Ga_{22}$ ribbons are just slightly higher than room temperature, i.e., $M_s = 323$ K, $M_f = 308$ K, $A_s = 318$ K and $A_f = 331$ K. The martensitic transformation should occur after the formation of final austenite microstructure, since it is impossible to realize the grain growth of austenite through interface movement at such low temperatures. Thus, we believe that the preferred orientation for the austenite in two ribbon samples should be in good agreement. The formation of preferred orientation for the austenite ($\{400\}_A$ parallel to ribbon plane) has also been confirmed in other NiMn-based alloys with different composition [18,23].

In our previous study, the orientation relationship between austenite and 7 M martensite has been revealed to be Pitsch relation with $\{101\}_A//\{1\bar{2}\bar{1}0\}_{7M}$ and $\langle 10\bar{1}\rangle_A//\langle\bar{1}0\bar{1}01\rangle_{7M}$ [24]. The crystallographic correlation between austenite and 7 M martensite can be well constructed by such a orientation relation. Accordingly, the possible orientations of martensitic variants (G^k_{7M}) with respect to the sample coordinate system can be calculated from a given orientation of austenite (G^l_A) by the following equation [24]:

$$G^k_{7M} = G^l_A \cdot S^j_A \cdot T^{-1} \cdot \left(S^i_{7M}\right)^{-1} \quad (1)$$

where T is the rotation matrix transforming the orthonormal crystal coordinate system fixed to the monoclinic martensite lattice to the austenite lattice basis; S^i_{7M} ($i = 1, 2$) and S^j_A ($j = 1,2,\ldots,24$) are the respective monoclinic and cubic symmetry elements. Here, an ideal austenite orientation with Euler angles of (0°, 0°, 0°) can be viewed as a typical representation for the orientation components of $\{400\}_A$//ribbon plane. To analyze the orientation correlation between austenite and 7 M martensite, the corresponding pole figures of two phases were calculated. Fig. 5a shows the $\{400\}_A$ pole figures for the austenite with ideal orientation of Euler angles (0°, 0°, 0°). Fig. 5b presents the corresponding resultant $\{20\bar{2}0\}_{7M}$, $\{2020\}_{7M}$, and $\{040\}_{7M}$ pole figures of the 7 M martensite variants recalculated with Eq. (1). It is shown that there exists an intimate correlation between $\{400\}_A$ and its resultant $\{20\bar{2}0\}_{7M}$, $\{2020\}_{7M}$, and $\{040\}_{7M}$, since the poles of $\{20\bar{2}0\}_{7M}$, $\{2020\}_{7M}$, and $\{040\}_{7M}$ are almost located at the same positions with those of $\{400\}_A$. Therefore, the martensitic transformation from austenite to 7 M martensite exhibits a strong orientation inheritance, which should be attributed to the intrinsic orientation relationship between austenite and 7 M martensite.

On the other hand, since the magnetic shape memory effect is strongly dependent on the distribution of martensite variant, the highly textured martensite microstructure favors the attainability

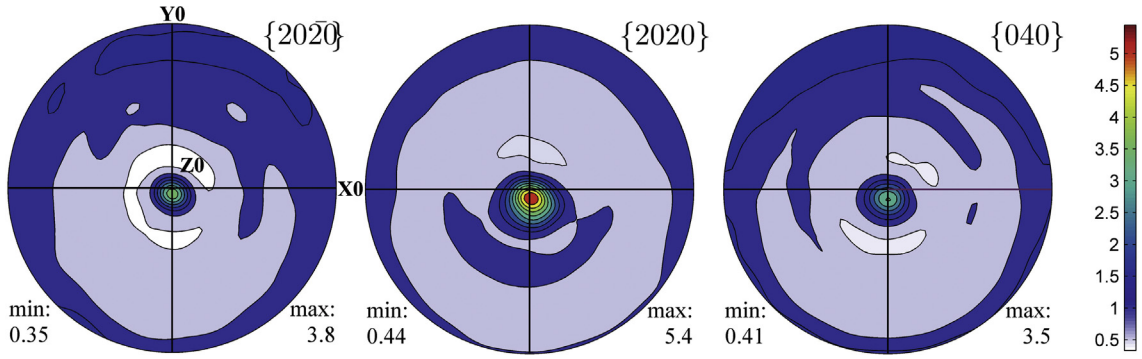

Fig. 4. $\{20\bar{2}0\}_{7M}$, $\{2020\}_{7M}$, and $\{040\}_{7M}$ pole figures recalculated from the XRD measurements for $Ni_{51}Mn_{27}Ga_{22}$ ribbons. X0//ribbon length (rolling) direction, Z0⊥ribbon plane.

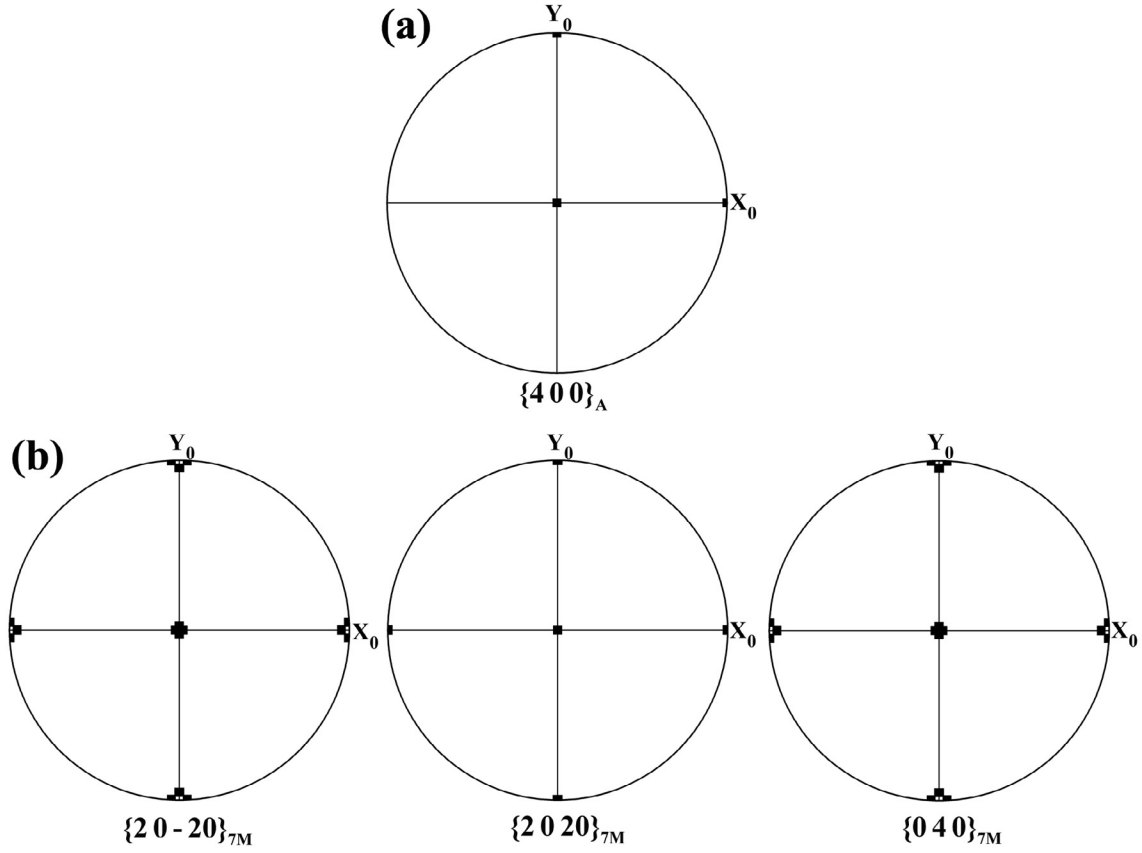

Fig. 5. (a) $\{400\}_A$ pole figure of austenite with Euler angle of (0°,0°,0°). (b) $\{20\bar{2}0\}_{7M}$, $\{2020\}_{7M}$ and $\{040\}_{7M}$ pole figure of 7 M martensite recalculated from austenite with the Euler angle of (0°,0°,0°) according to Pitsch relation.

of the field induced output. Due to the fact that the crystallographic texture exhibits a strong inheritance during the martensitic transformation, the crystallographic texture of product martensite should be determined by that of parent austenite. The formation of highly textured microstructure in parent austenite would greatly promote the orientation uniformity of the martensite. Thus, from the point of property optimization, formation of highly textured parent austenite is a necessary prerequisite to the orientation control of martensite in polycrystalline alloys.

Conclusions

In summary, the preferred orientation distribution for the austenite in $Ni_{53}Mn_{22}Ga_{25}$ ribbons and the 7 M martensite in $Ni_{51}Mn_{27}Ga_{22}$ ribbons was studied. It is found that the austenite forms a preferred orientation with $\{400\}_A$ in parallel to ribbon plane, whereas the 7 M martensite develops the preferred orientation with $\{20\bar{2}0\}_{7M}$, $\{2020\}_{7M}$, and $\{040\}_{7M}$ crystallographic planes parallel to the ribbon plane. Furthermore, the preferred orientation distribution for austenite and 7 M martensite was well correlated and the preferred orientation in ribbons can be inherited after the martensitic transformation. Such texture inheritance is attributed to the intrinsic orientation relationship between austenite and 7 M martensite.

Acknowledgements

Financial supports from National Natural Science Foundation of China (Grant Nos. 51431005, 51571056), the 863 Program of China (Grant No. 2015AA034101), the 111 Program of China (Grant No.

B07015), the Fundamental Research Funds for the Central Universities of China (Grant No. N130110001), the PhD Starting Foundation of Liaoning Province (Grant No. 20141001) and the Funding Program of the Education Department of Liaoning Province (Grant No. L2014094) are highly appreciated. Z. B. Li is grateful to the French State through the Investment in the Future Program operated by the National Research Agency and referenced by ANR-11-LABX-0008-01 (LabEx DAMAS) for the invited professorship.

References

[1] Dunand DC, Müllner P. Adv Mater 2011;23:216–32.
[2] Planes A, Mañosa L, Acet M. J Phys: Condens Matter 2009;21:233201.
[3] Li Z, Xu K, Zhang Y, Tao C, Zheng D, Jing C. Sci Rep 2015;5:15143.
[4] O'Handley RC. J Appl Phys 1998;83:3263–70.
[5] Cong DY, Roth S, Schultz L. Acta Mater 2012;60:5335–51.
[6] Huang L, Cong DY, Wang ZL, Nie ZH, Dong YH, Zhang Y, Ren Y, Wang YD. J Phys D: Appl Phys 2015;48:265304.
[7] Pagounis E, Chulist R, Szczerba MJ, Laufenberg M. Appl Phys Lett 2014;105:052405.
[8] Pagounis E, Szczerba MJ, Chulist R, Laufenberg M. Appl Phys Lett 2015;107:152407.
[9] Sozinov A, Lanska N, Soroka A, Zou W. Appl Phys Lett 2013;102:021902.
[10] Li ZB, Zhang YD, Sanchez-Valdes CF, Sanchez Llamazares JL, Esling C, Zhao X, Zuo L. Appl Phys Lett 2014;104:044101.
[11] Li ZB, Sánchez Llamazares JL, Sánchez-Valdés CF, Zhang YD, Esling C, Zhao X, Zuo L. Appl Phys Lett 2012;100:174102.
[12] Hernando B, Sánchez Llamazares JL, Prida VM, Baldomir D, Serantes D, Ilyn M, González J. Appl Phys Lett 2009;94:222502.
[13] Rama Rao NV, Gopalan R, Manivel Raja M, Arout Chelvane J, Majumda B, Chandrasekaran V. Scr Mater 2007;56:405.
[14] Liu J, Woodcock TG, Scheerbaum N, Gutfleisch O. Acta Mater 2009;57:4911.
[15] Hernando B, Sánchez Llamazares JL, Santos JD, Escoda LI, Suñol JJ, Varga R, Baldomir D, Serantes D. Appl Phys Lett 2008;92:042504.
[16] Sánchez Llamazares JL, Sanchez T, Santos JD, Pérez MJ, Sanchez ML, Hernando B, Escoda LI, Suñol JJ, Varga R. Appl Phys Lett 2008;92:012513.
[17] Sánchez Llamazares JL, Hernando B, García C, González J, Escoda LI, Suñol JJ. J Phys D: Appl Phys 2009;42:045002.
[18] Liu ZH, Chen JL, Hu HN, Zhang M, Dai XF, Zhu ZY, Liu GD, Wu GH, Meng FB, Li YX. Scr Mater 2004;51:1011–5.
[19] Li ZB, Zou NF, Sánchez-Valdés CF, Sánchez Llamazares JL, Yang B, Hu Y, Zhang YD, Esling C, Zhao X, Zuo L. J Phys D: Appl Phys 2016;49:025002.
[20] Hielscher R, Schaeben H. J Appl Cryst 2008;41:1024–37.
[21] Li ZB, Zhang YD, Esling C, Zhao X, Wang YD, Zuo L. J Appl Cryst 2010;43:617–22.
[22] Jiang C, Liu J, Wang J, Xu L, Xu H. Acta Mater 2005;53:1111–20.
[23] Li ZB, Wang JJ, Zhang YD, He KZ, Zhao X, Zuo L, Hofer G, Esling C. Adv Eng Mater 2010;10:1024–8.
[24] Li ZB, Zhang YD, Esling C, Zhao X, Zuo L. Acta Mater 2011;59:2762–72.